3D Printing of Optical Lenses Assisted by Precision Spin Coating

Yujie Shan†*, Junyu Hua* †*, and Huachao Mao**

Y. Shan, J. Hua, Dr. H. Mao
School of Engineering Technology, Purdue University, West Lafayette, IN 47906, USA
E-mail: mao145@ purdue.edu
†These authors contributed equally to this work.

Keywords: 3D printing, vat photopolymerization, unfocused image, optical lens, spin coating

Abstract

Though 3D printing shows potential in fabricating complex optical components rapidly, its poor surface quality and dimensional accuracy render it unqualified for industrial optics applications. The layer steps in the building direction and the pixelated steps on each layer's contour result in inevitable microscale defects on the 3D-printed surface, far away from the nanoscale roughness required for optics. This paper reports a customized vat photopolymerization-based lens printing process, integrating unfocused image projection and precision spin coating to solve lateral and vertical stair-stepping defects. We demonstrate a precision aspherical lens with less than 1 nm surface roughness and 1 μm profile accuracy. The 3D-printed convex lens achieves a maximum MTF resolution of 347.7 lp/mm. We establish a mathematical model to predict and control the spin coating process on 3D-printed surfaces precisely. Leveraging this low-cost yet highly robust and repeatable 3D printing process, we showcase the precision fabrication of multi-scale spherical, aspherical, and axicon lenses with sizes ranging from 3 mm to 70 mm using high clear photocuring resins. Additionally, molds were also printed to form multi-scale PDMS-based lenses. Following precision polishing, precision machining, and precision molding, we anticipate that precision spin coating will empower 3D printing as the fourth generation of lens making and unleash the power of 3D-printed lenses in rapid and massive customization of high-quality optical components and systems.

Introduction

Optical lenses are the foundational elements in nearly all systems that utilize lights, for instance, imaging systems for microscope and telescope, illuminating systems, manufacturing systems for laser beam delivery, human and machine vision, and the virtual and mixed reality display for metaverse [1,2]. Generally, the fabrication of these versatile lenses is a sophisticated process, involving the precise shaping, polishing, and assembly of transparent materials to manipulate light. A sequence of time-consuming processes are utilized, such as grinding, polishing, molding, and coating, each of which is critical in achieving the desired optical properties and quality for lenses [3]. The revolution of optical systems often comes with the advance of manufacturing processes. Polishing enabled the first generation of telescopic optics centuries ago. Precision CNC machining was a giant leap to modernize aspheric and freeform lenses decades ago. Precision molding of lenses democratized the wider use of optic lenses, empowering the cameras in electronics, such as cell phones, computers, machine vision, and artificial intelligence (AI) years ago [3–5].

Additive manufacturing, or 3D printing, will be potentially the fourth generation of lens making, leading to rapid lens fabrication that facilitates quick and cost-effective lens prototype development, while also expediting innovation and customization across industries, including custom eyewear, vision correction devices, scientific instrumentation, and medical devices. Additive manufacturing is a process of creating physical objects by layering material based on a Computer-Aided Design (CAD) model [6,7]. Its function has quickly expanded from prototyping into manufacturing complex parts, which is difficult to do with conventional techniques such as freeform lenses [8–11]. Among all additive manufacturing processes, material jetting is the early commercialized process for lens making, due to the benefit of jetting different types of materials into a single part [12]. But material jetting is slow and limited to water-like less-viscous materials. In comparison, vat photopolymerization (VPP) is commonly used for optical applications due to high precision, fast printing speed, multiple material selections [13–15], and affordable imaging light sources[16] [17] [18]. Recent studies demonstrated printing lenses in minutes using vat photopolymerization [19,20]. Besides, additive manufacturing enables geometric lenses with extra functions. For instance, Alam et al. 3D-printed personalized smart contact lenses with enhanced features, such as built-in sensors and custom textures, offer advantages over traditional methods [21,22]. In this regard, additive manufacturing will revolutionize traditional manufacturing processes [3–5], provide newfound flexibility, precision, and functionality, and accelerate lens fabrication timelines across multiple applications [23–26].

Though promising in lens making, additive manufacturing is challenged to fabricate optically smooth surfaces due to fundamentally inevitable stair-stepping defects: laterally pixelated steps within a layer (Fig. 1c) and vertically layered steps along the building direction (Fig. 1e) [27–29]. Various attempts have been made to mitigate these step defects. For the lateral staircase within a layer, researchers used the grayscale exposure to blur the pixel aliasing and smoothen the curved contour in one layer [30]. Reducing the size of each pixel [31,32] is another approach to smoothen the printed layer. However, reduced pixel size decreased the building size to several millimeters. The authors used unfocused images to smoothen the pixelation defects, without sacrificing the building size [27], which was adopted in this work. For layered steps, Chen et al. proposed a VPP process that combines grayscale exposure with a meniscus post-curing technique, and printed aspherical lenses with a surface roughness as low as 7 nm [31]. Zhang et al. introduced continuous liquid interface production (CLIP) 3D printing to fabricate contact eye lenses with a single droplet resin [33]. Xu et al. introduced a cost-effective volumetric 3D printing technique that rapidly and precisely creates miniature lenses with sub-nanometric roughness, suggesting its potential for large-scale precise lens production [34]. Meniscus coating is a common post-processing to reduce the vertical steps [31,35], but it cannot eliminate the steps and the dimensional accuracy is hard to reach the requirement of optical elements. In addition, the standard deviation in the peripheral region using the drop coating method was much higher than expected, which largely affected lens fabrication quality. Some researchers utilized other post-processing methods such as grinding, polishing, and glass curing to obtain a transparent and smooth surface after 3D printing [36,37], but these processes are time-consuming and the limited repeatability accuracy makes them unsuitable for mass fabrication. Continuous printing [16,20,38] eliminated the layered steps in the building direction. However, the printed surface is still not smooth due to the pixelated mask images. Besides continuous printing is limited to thin-walled structures for the sake of resin refilling, while most lenses are solid with large cross sections. Some other novel 3D printing techniques were developed and conducted for high-quality optics fabrication, but the printing size is limited [39–43]. Despite all these tremendous efforts, it is still lacking an effective and efficient method to eliminate the stair-stepping defects vertically and laterally.

In this study, we present a method that is both time-efficient and cost-effective to produce high-quality optical lenses. We first used vat photopolymerization with an LCD light source to fabricate a layered three-dimensional lens[15] (Fig. 1a and 1b). By slightly defocusing the curing image [27] in Fig. 1d, the lateral pixelated can be largely solved, as shown in Fig. 1e and

1f. Then, spin coating was used to smoothen the layered steps along the building direction, which is shown in Fig. 1g. Previously, spin coating on a curved surface was believed to be an unpredictable and unrepeatable process. However, this work shows the opposite: spin coating on printed surfaces can be precisely controlled, creating a highly robust and predictable coating profile. In this paper, we experimentally, numerically, and mathematically modeled the coating process and its effect on the lenses' smoothness and accuracy. For the first time, we achieved sub-micron precision spin coating on 3D-printed surfaces and obtained the theoretical conditions for such precision. Supplementary Table 1 compares our work with existing 3D printing methods in terms of fabrication ability, optical performance, and surface characterization [19,20,31,33,34,36,37,39–43].

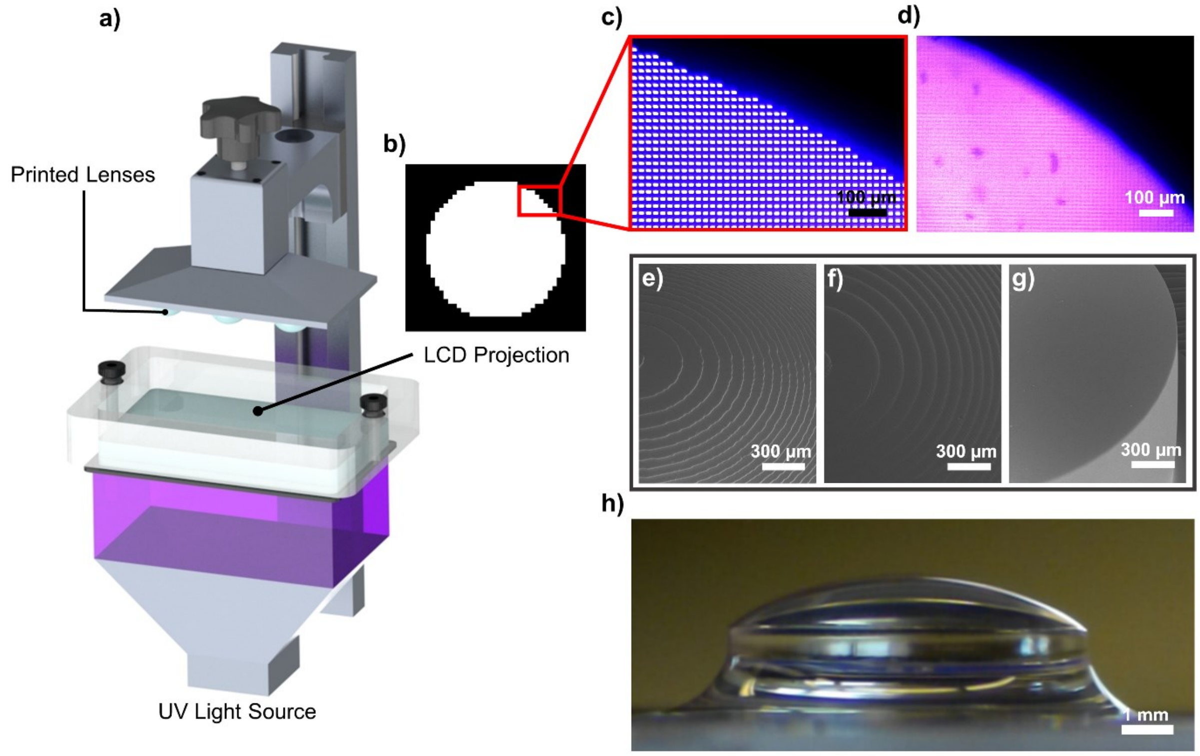

Figure 1. a) VPP-based 3D printing setup. b) Projection image for a single printing layer. Light intensity of focused image (c) and unfocused image (d). SEM images of printed samples using focused image (e) and unfocused image (f), and after the spin coating process (g). h) 3D printed lens by utilizing the unfocused image and the precision spin coating.

We demonstrated 3D-printed multi-scale singlet lenses ranging from 3 mm to 70 mm and experimentally characterized their optical performances. Various types of lenses, such as aspheric and axicon lenses, were also printed and tested to verify the effectiveness of our method. Beyond photocurable resins, other optical materials such as PDMS were molded into lenses by 3D printing a negative mold. Like precision polishing, precision machining, and precision molding, we anticipate that precision spin coating will empower additive manufacturing as the fourth generation of lens making and unleash the power of 3D-printed lenses in rapid and massive customization of optics.

Results

Fabrication Method

Figure 2 illustrates our strategy to fabricate optical components based on VPP 3D printing and the spin coating process. In Fig. 2a, we customized a 3D printing system utilizing an LCD-based mask with a bottom-up projection mechanism. This system incorporates a Liquid Crystal Display (LCD) screen to selectively project the sliced 2D images to cure the liquid resins in the vat. A 150 µm-thick Teflon releasing film is attached to the vat's base to ease the separation between cured resin with the film. Furthermore, a glass slide was used as the building platform to hold the printed part, leading to a flat surface of the printed lens.

To provide backlighting for the LCD panel, a powerful UV LED light source is requested. However, most of the light is obstructed when the UV light meets the boundaries of the LCD transistors. This phenomenon manifests as a grid-type shadow, as depicted in Fig. 1c. Such dark grids contribute to pixel disconnection and uneven light intensity distribution, ultimately producing staircase defects on each lateral layer printing. By manipulating the LCD screen's movement in the printing direction, we can project an unfocused image pattern, enhancing the smoothness of the printed structures for individual layers, as illustrated in Fig. 1d. The SEM image in Fig. 1e highlights the staircase effect observed in samples produced using conventional focused image projection. In contrast, our innovative approach facilitates the printing of intricate curved structures in the lateral direction, as demonstrated in Fig. 1f.

To eliminate the vertical stair-stepping effect, we proposed a fabrication flow including the spin coating and vacuum post-curing in Fig. 2b. The printed lens sample on a glass slide was first peeled off from the building platform and centered on the spin coater. After dropping sufficient clear resin to cover the sample's entire surface, we conducted a spin coating process with 1000 rpm for 20 seconds. The residual resin was distributed uniformly on the outer surface and covered the staircase of the printed sample. Then the lens sample was moved to a vacuum chamber for post curing, which avoided the curing inhibition effect induced by oxygen and removed potential bubbles inside the coated thin layer of fresh resin. A powerful

UV lamp was mounted to cure the coated sample for 40 seconds. Finally, an optical lens was fabricated as shown in Fig. 1h and Fig. 2c.

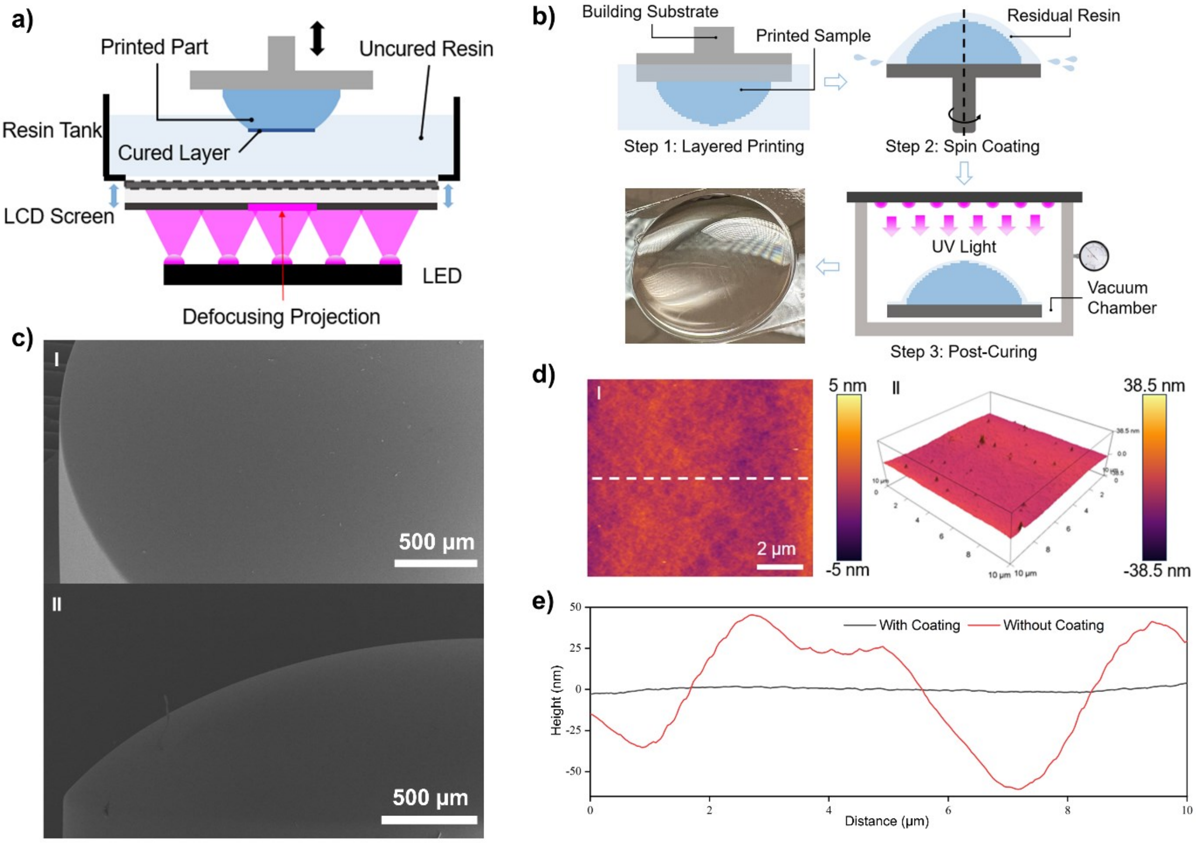

Figure 2. a) Schematic illustration of the 3D printing system. b) Fabrication flow including spin coating and post-curing processes. c) SEM images of fabricated lens. d) AFM top surface 2D (I) and 3D (II) images of the fabricated lens. e) Comparison of measured height profile along the marked dashed line between the lens samples with and without the coating process.

Precision spin coating is a critical step in the above lens fabrication. Compared with drop coating with gravity only, spin coating has three benefits. First, spin coating enables the coating of the concave lens by using centrifugal force to drain out the resin in the concave lens, whereas the resin will be stuck in drop coating. Second, spin coating is much faster than drop coating. Supplementary Figure 2 shows that a couple of hours are required for drop coating to drain out the resin while spin coating only needs tens of seconds. Thirdly, our simulation shows that the spin coating leads to a more uniform coating with sub-microns' variation in the thickness through the major portion of a spherical lens. In comparison, drop coating yields about eight micrometers' deviation in coating thickness across the lens. Additionally, atomic force microscopy (AFM) measurements in Fig. 2d reveal that the 2D and 3D surface images of our printed sample over a 10 × 10 μm sampled area after spin coating treatment. Figure 2e shows the measured height profile along the marked dashed line with and without spin-coated samples. For comparison, the 2D and 3D AFM surface images of the printed lens (washed) without the spin coating were shown in Supplementary Fig. 3a and 3b. Multiple locations on two samples were tested, and the average surface roughness (RMS) of our lens sample was about 0.639 nm within the measured area (Supplementary Fig. 3c and 3d).

Optical Characterization of 3D-Printed Lenses

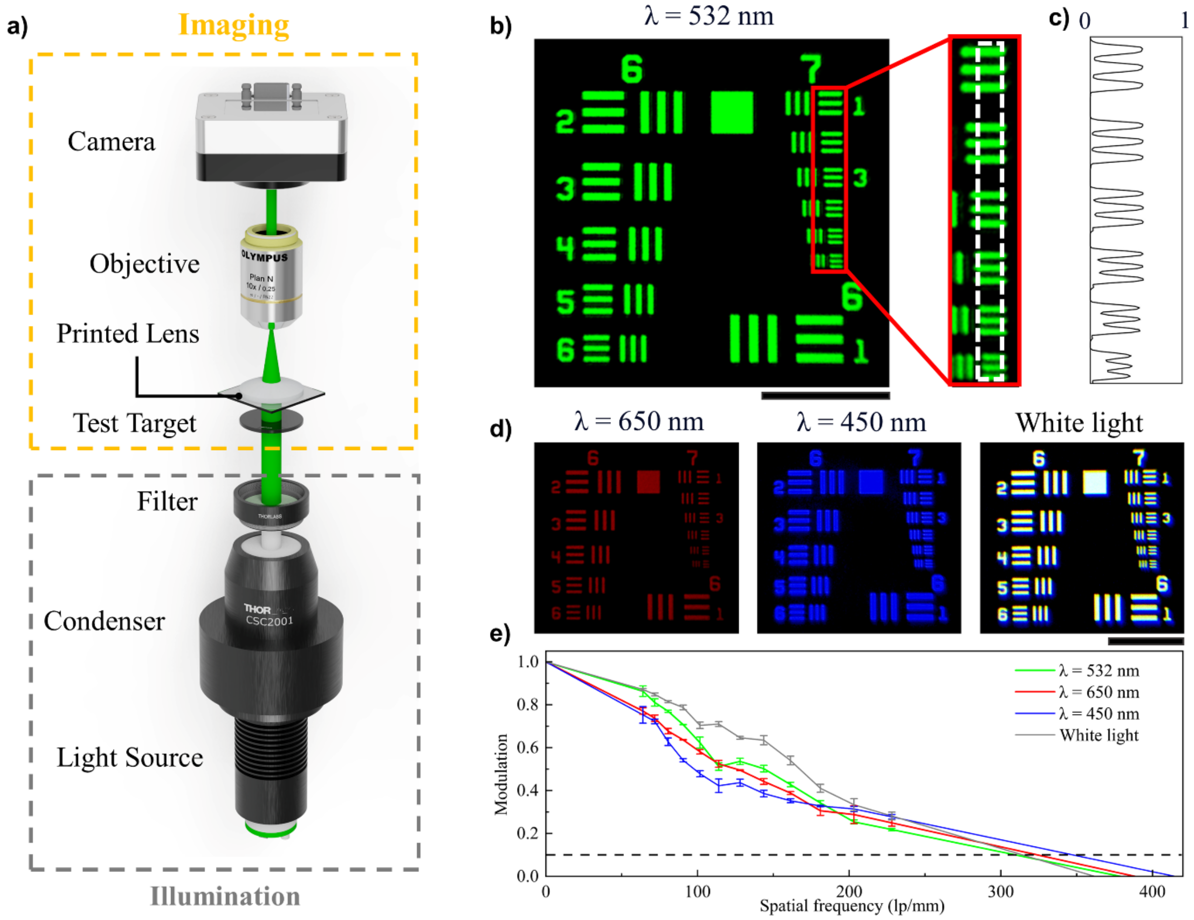

Figure 3. a) Schematic illustration of the testing system. b) Captured USAF 1951 target image at 532 nm wavelength (green light). c) Intensity profile at the marked position. d) Captured USAF 1951 target images at 650 nm wavelength (red light), 450 nm (blue light), and white light. e) Measured MTF for the testing lens under different lights. Scale bars: 100 µm.

Figure 3a displays the setup used to evaluate the optical performance of the 3D-printed lens, imaging a negative United States Air Force (USAF) 1951 resolution test target under various illumination wavelengths. We captured images with the fabricated lenses using a 4× objective lens (AmScope LLC) and a USB color CMOS digital microscope camera (MD130, AmScope LLC). To achieve different color illuminations, we employed multiple bandpass filters from

Thorlabs, Inc., including the wavelengths centered at 450 nm (blue), 532 nm (green), and 650 nm (red). The imaging system's aperture was 3 mm. When imaging under green light, we successfully observed Group 7 on the test target, as shown in Fig. 3b. The average intensity profile of the magnified region was graphed (Fig. 3c), revealing a distinct modulation in the captured image. Additionally, we imaged the target using red, blue, and white light illumination (400–800 nm) to assess the broadband performance, as shown in Fig. 3d. We then calculated the modulation transfer function (MTF) and a 10% modulation threshold in the MTF was used to determine the imaging resolution. Figure 3e indicates the imaging resolution at spatial frequencies of 309.7, 324.1, 347.7, and 314.4 lp/mm under green, red, blue, and white light illumination, respectively.

Imaging experiments

To briefly showcase potential applications, we used the setup in Fig. 3 and coupled it with our 3D-printed singlet lens to image different samples. The lens's ability to capture vivid colors was demonstrated in Fig. 4a–f. The vibrant details of the Zea Stem, Lilium Ovary, Honeybee Wing, Fruit of Ficus Carica, and Fish Gill, and an Ant were imaged, demonstrating the superior optical quality of our printed lens. These evaluations collectively affirmed that the 3D-printed lens with standard cameras delivered not only sharp images but also minimal distortion across a wide visible range.

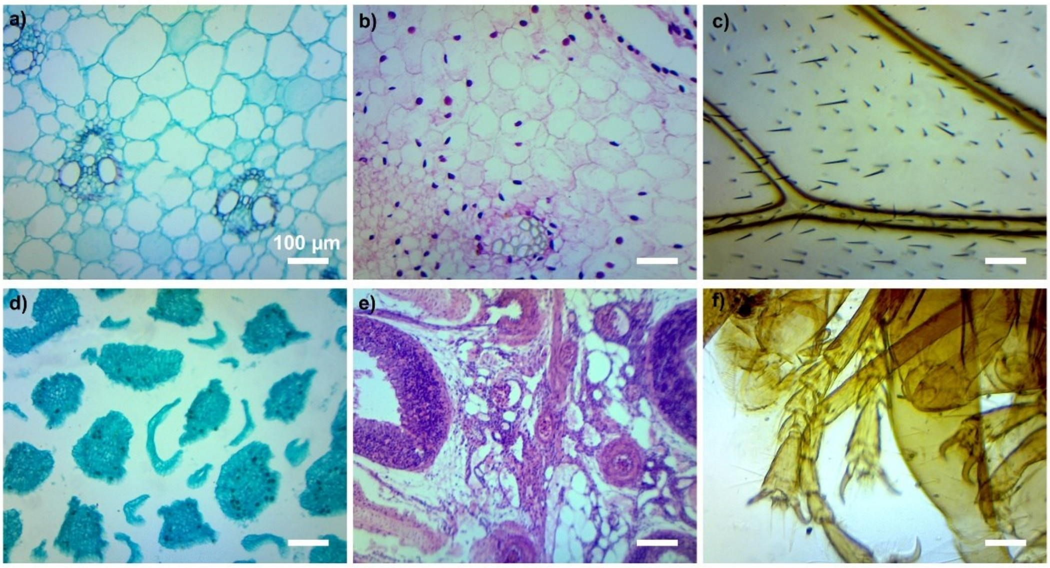

Figure 4. Image of a Zea Stem a), a Lilium Ovary b), a Honeybee Wing c), a Fruit of Ficus Carica d), a Fish Gill e), and an Ant f). Scale bars: 100 µm.

Multi-Scale Multi-Type Lenses

Using our proposed method, we have fabricated lenses of varying dimensions with the benefit of 3D printing in peed and structural customization. As depicted in Fig. 5a, we printed multi-scale spherical lenses with distinct diameters of 3mm, 6mm, 12.7mm, and 25.4mm using our customized and commercial clear resins. Lenses of larger sizes were also shown in Supplementary Fig. 4a. These results show that the printed lenses exhibited commendable surface roughness and imaging properties. To further validate the versatility of our technique, we printed aspherical lenses, as presented in Fig. 5c. In Fig. 5d, the printed axicon lenses demonstrated superior imaging outcomes, using the testing equipment and optical system elaborated in Supplementary Fig. 5. Utilizing the same printing methodology, we printed molds in a concave shape and subsequently combined the spin-coating and the post-processing. The mold shows excellent surface roughness and a controllable profile precision. Using this mold, we successfully fabricated lenses from PDMS material via casting. Fig. 5e illustrates the molded, flexible PDMS lens. The detailed fabrication flow of PDMS-based lenses can be found in Supplementary Fig. 6.

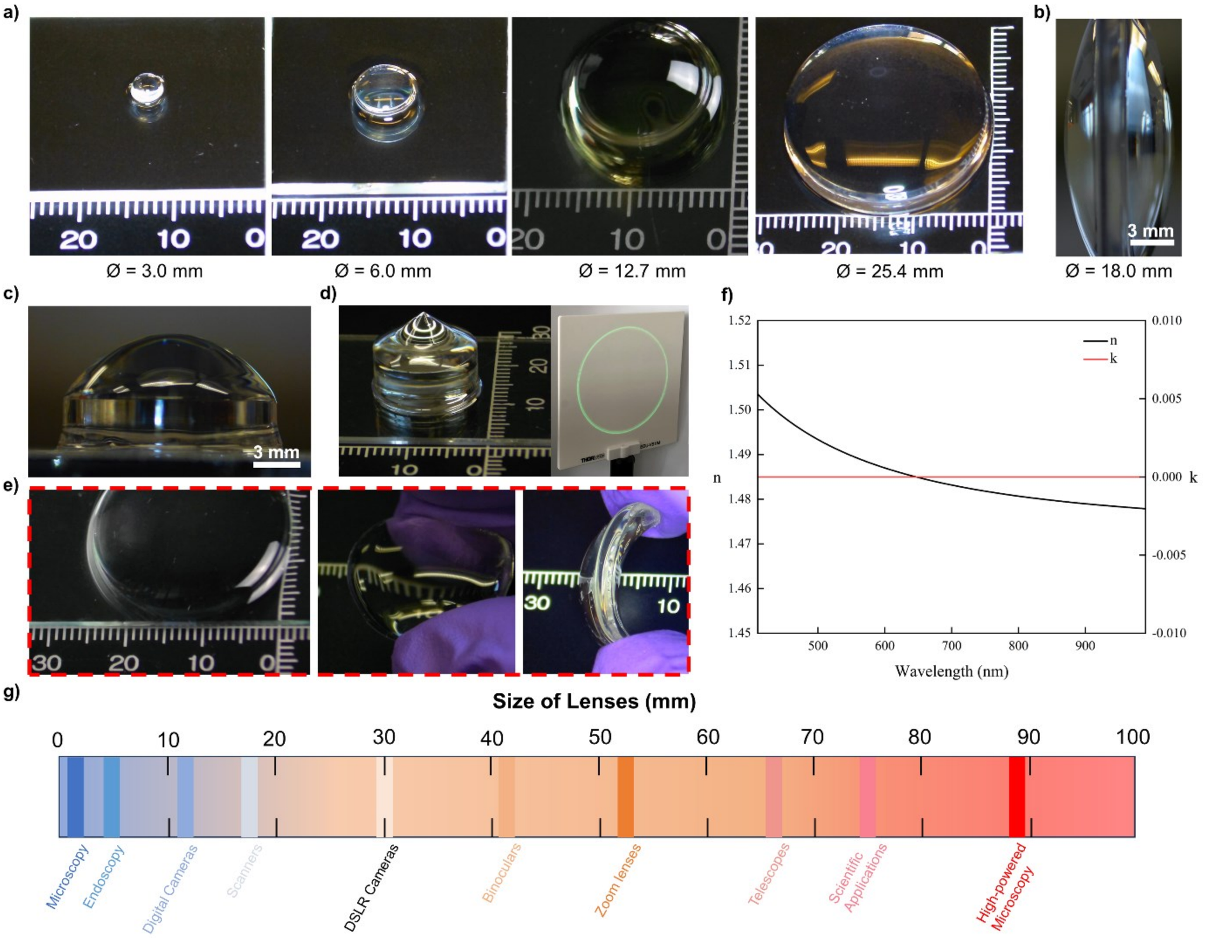

Figure 5. a) Multi-scale printed lenses. b) Printed bi-convex lens. c) Printed aspherical lens and axicon lens. d) Printed axicon lens. e) PDMS-based lenses. f) Complex refractive index of high clear

resin (cured for 20s) in different wavelengths. g) A summary of applications of different-size lenses that our method can print.

Figure 5f displays the refractive index variations of the high clear resin we employed with a 40-second post-curing time, across different wavelengths, which was measured by a Spectroscopic Ellipsometer (RC2, J.A. Woollam). The refractive indexes of some other photo-curing resins are also illustrated in Supplementary Fig. 7a. Additionally, the transmittance of our printed resins were measured by a Spectrophotometer (Supplementary Fig. 7b). These spectral characteristics data can be instrumental for the optical system analysis and simulation of the lenses we crafted. Figure 5g summarizes the applications corresponding to lenses of different sizes in microscopy, medical devices, telescopes, cameras, and scientific devices. This emphasizes the significance of rapid lens fabrication across multiple sizes in industries.

Precision Spin Coating

Usually, spin coating on a curved surface is viewed as an unpredictable and unrepeatable process. However, our modeling and experiments show the opposite: spin coating on printed surfaces can be accurately controlled, creating a highly robust and predictable coating profile. We experimentally, mathematically, and numerically model the coating process to understand the effect of coating on the profile's smoothness and accuracy.

We obtained three significant results for spin coating on 3D-printed aspherical lenses:

(1) The coating on a 3D-printed surface is equivalent to coating on a smooth spline interpolating all printing layers' corner points.

We found that printed stairs will not affect the profile if the amount of liquid is larger than the volume of the triangled staircases. In spin coating, the liquid is shaped by four forces: surface tension, centrifugal force, gravity, and viscous force. Among them, surface tension quickly forces the liquid to form a smooth surface within a split millisecond, while the gravity and centrifugal force act much slower in terms of seconds. Such phenomena lead to the solution being insensitive to the staircases, as the surface tension swiftly smoothens the printed layer steps and always stays in hydrostatic equilibrium. In Supplementary Fig. 8, the initial profile is set as zig-zag uneven. After only ten microseconds, the zig-zag profile flattens. This result was also validated in our physical experiments. Figure 6a shows that the coating profile of a printed sample was smooth even when the liquid barely covered the printed layer steps.

Therefore, we conclude that the stairs will not affect the profile if the amount of liquid is larger than the volume of the triangled staircases. Based on this result, we can simply treat the 3D-printed surface as a smooth substrate spanned by all steps' corners.

(2) **Coating thickness is insensitive to the initial thicknesses and can be analytically predicted as a function of time and lens profile**.

We simulated the coating profile under various initial thicknesses, as shown in Supplementary Fig. 9. We found that regardless of the initial coating conditions, the coating profile converged to the same profile. Figure 6b shows the simulated coating profile as a function of time and location. Supplementary Figure 10 shows the coating thickness at the center quickly converged to the analytical solution, given three dramatically different initial thicknesses.

The converged profile can be analytically modeled as a function of time (t) and geodesic distance (s) from the point (r, z) to the center along the lens surface:

$$h(t,s) = \frac{1}{\sqrt{t + t_0}} f(s)^{-\frac{1}{3}} \sqrt{\int_0^s r(s) f(s)^{-\frac{1}{3}} ds} \tag{1}$$

where,

$$\begin{gathered} f(s) = \frac{\rho(\omega^2 r^2 \cos\theta + rg\sin\theta)}{\eta}. \\ t_0 = \frac{0.75\eta}{\rho \mathrm{h}_0^2(\omega^2 + g/R)} \end{gathered} \tag{2}$$

As shown in Fig. 6c, R is the radius of curvature at the center, h_0 is the initial height in the center point's coating thickness, ω is the spin speed, and ρ, η are the density and viscosity of the coating liquid. The detailed deduction of these equations refers to Supplementary Notes S1 and S2. The calculated coating profile as a function of time and geodesic distance was also demonstrated (Fig. 6c). The MATLAB code to calculate the coating profile for any aphserical lens will be available via GitHub.com.

The simulated profile accurately overlaps with the analytical models as shown in Fig. 6d. Figure 6e shows our analytical results also matched the experimental measurements. In our experiments, the radius was 15 mm, and the spin speed as 1000 rpm. We measured the rheological properties of the liquid resin (Newtonian fluid) as shown in Fig. 6f. The viscosity of our resin was obtained as 0.370 Pa·s by calculating the slope of this straight line. $\eta =$

$0.370\ Pas$, and $\rho = 1090\ kg/m^3$, and $h_0 = 1mm$. $t_0 = 0.75 * \frac{0.370}{1090*0.001^2*\left(104.7^2+\frac{9.8}{0.015}\right)} s = 0.022s$. We spin-coated for 20 seconds, which is 1000 times larger than t_0.

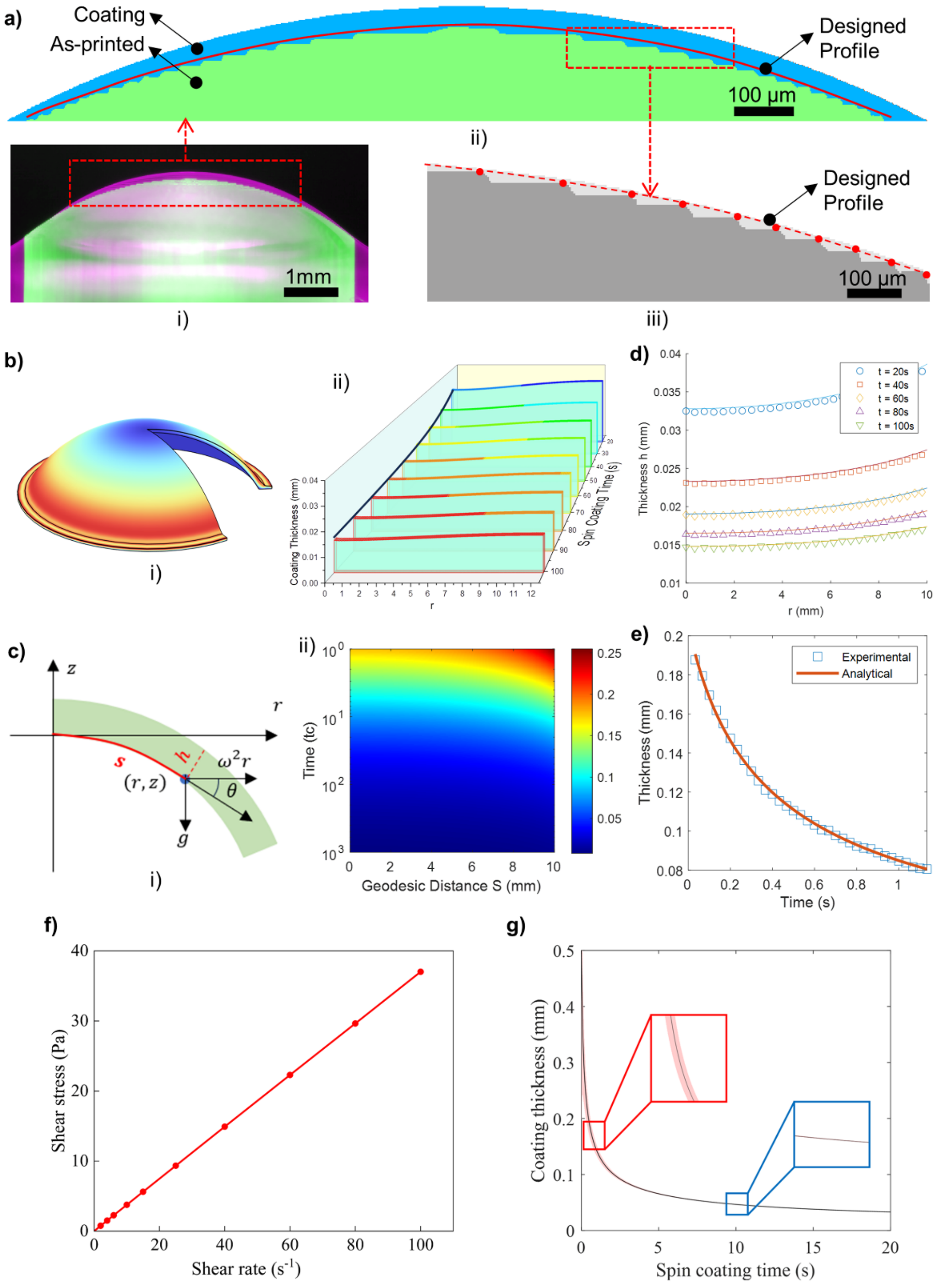

Figure 6. Experimental, numerical, analytical modeling and accuracy of spin coating. a) Experimental measurement of spin coating. b) Numerical modeling. (i) COMSOL simulations of spin coating. (ii) Coating thickness as a function of distance and coating time. c) (i) Analytical modeling. (ii) Analytical prediction of coating thickness as a function of geodesic distance and time. d) Simulated thickness agrees with analytical thickness. e) Analytical prediction of the thickness in the lens center agrees well

with the experimental measurement. f) Shear stress–shear rate curve for the high clear resin in our printing. g) Coating thickness variation under different conditions.

(3) **The accuracy of coating thickness can be controlled within 1 μm**.

Consider initial thickness at center ranges from h_0 to h_1. Then the percentage variation of coating thickness is bounded as

$$\frac{\Delta h(t)}{h(t)} = \frac{t_0}{2t} \tag{3}$$

$\frac{\Delta h(t)}{h(t)} = \frac{t_0}{2t}$where $t_0 = \frac{0.75\eta}{\rho \mathrm{h}_0^2(\omega^2+g/R)}$. The derivation of this equation is in Note S2.

In our physical experiments, the spin coating time was larger than 1000 times to $t_0 = \frac{0.75\eta}{\rho \mathrm{h}_0^2(\omega^2+g/R)}$. This leads to the temporal accuracy within 0.05% of the coating thickness, less than 0.02 μm for a coating thickness of 40 μm. This astonishing result shows that the variations of coating different samples were well controlled with 1 μm. In Fig. 6g, the effect of initial coating thickness was quickly mitigated. The variation of coating thickness under different conditions was reduced to submicron after 20 seconds and was further reduced to 10 nm after 90 seconds. The setup for capturing the profile of printed lenses is shown in Supplementary Fig. 5.

The modeling and simulation results verified two critical hypotheses: (1) the layer stair does not affect the coating profile, and (2) the initial amount of coating resin does not affect the coating profile after a critical spin time. These two results theoretically ensure the repeatability and reliability of the coating process. This predictable coating is the foundation for 3D printed lenses to have submicron level profile accuracy, comparable to most expensive lens fabrication processes, such as precision molding or CNC machining.

Dimensional Accuracy and Shape Compensation

To demonstrate the profile accuracy, we utilized a 3D Surface Metrology Microscope (Leica DCM8, Leica Microsystems), which unites the confocal microscopy and interferometry into one versatile. The 3D images were captured to analyze the surface profile accuracy of our lens samples. Figures 7a and 7b show the measured 3D shape of our lens samples. For comparison, the measured height profiles of samples were matched and shown in Fig. 7c. The average profile deviation (RMS) of our lens sample is 0.511 μm along the middle line.

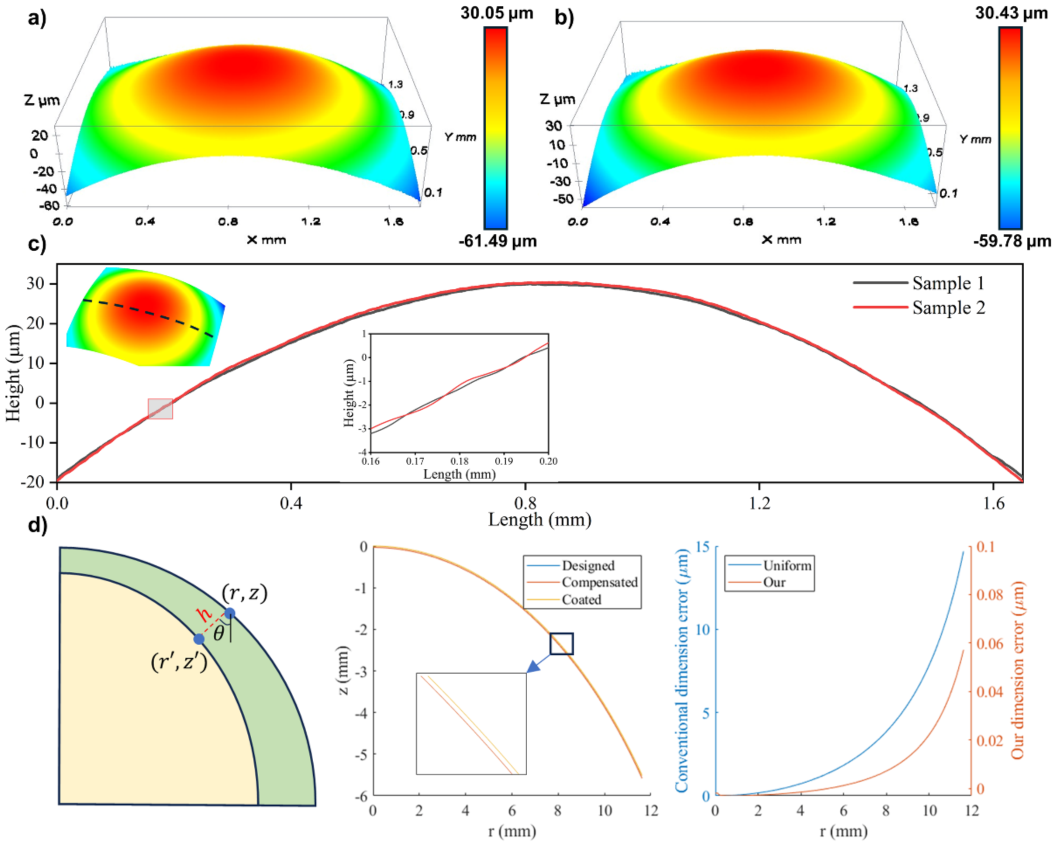

Figure 7: 3D surface profile images of the printed lenses a) and b). c) Comparison of the measured height profile along the marked dashed line between two samples. d) Coating thickness compensation under the designed dimensions.

Shape Compensation is needed to ensure the coated lens has the designed dimensions. However, the coating thickness is not uniform, and simply offsetting the lens profile with a constant thickness cannot yield the correct dimension. Instead, we leverage the Equation (1) to adaptively modify the lens profile. Given an aspherical surface profile $z = z(r)$, as shown in Supplementary Fig. 1a. Any point on the surface (r, z) is modified as:

$$\begin{aligned} r' &= r - h(t, r) \cdot \sin(\theta_r) \\ z' &= z - h(t, r) \cdot \cos(\theta_r) \end{aligned} \tag{4}$$

where $h(t, r)$ is the coating thickness at time t at the radius r, and θ_r is the surface angle at radius r. We have programed this shape compensation algorithm in MATLAB and made it available via Github.com. The Equation (1), the coating thickness of any location $h(t, r)$, is critical to guarantee the final dimensional accuracy. We compared the final dimension of the compensated and coated lens with the designed dimension in Figure 7d. The results show that the maximum profile error at the edge of the lens is less than 0.06 µm. In comparison, if we simply use a uniform coating thickness to compensate, the maximum profile error can reach 15 µm, which is hundreds of times larger than our method.

Functional Lenses

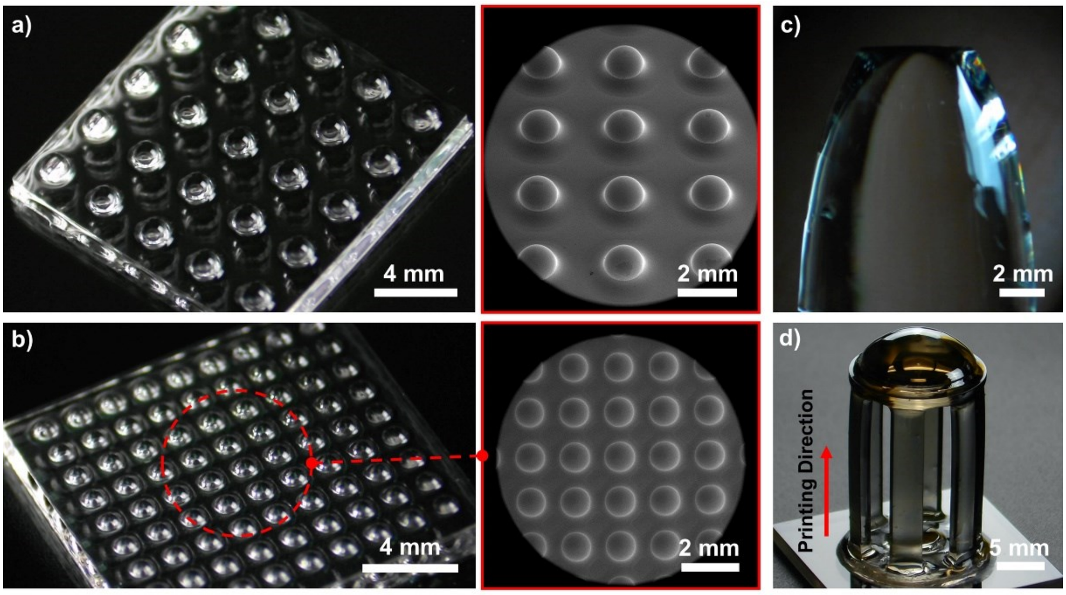

Figure 8. Functional lenses printing: Microlens array sample a) and b). c) Printed compound parabolic concentrator (CPC) element. d) Printed laser beam expander after gold sputter coating.

We demonstrate the feasibility and performance of our proposed technique by fabricating customized functional optical lenses. As depicted in Fig. 8a and 8b, we printed microlens array with the diameter of 1.5 mm and 0.8 mm. After spin coating along object's central line, the microlens array has been fabricated with excellent surface quality and uniform dimensions, as investigated in SEM images. In Fig. 8c, a compound parabolic concentrator (CPC) element was printed with a large acceptance angle of 45° and featuring a 5 mm exit diameter. This functional lens can efficiently collect and concentrate light onto a smaller receiver, ideally used in solar energy systems. The dimensions are based on a commercial lens (17-710, Edmund Optics). In addition, we demonstrate the capability of our method in directly fabricating an assembled lens set. A Keplerian laser beam expander with a magnification ratio of 1:2 was designed and printed in Fig. 8d. This lens set was horizontally placed on the building platform and printed along the moving direction. To avoid the overcuring issues on overhanging structures printing, the curing time for each layer on overhanging region was modified and more rest time was also added. The detailed printing parameters can be found in Supplementary Table 3. Another lens set sample with vertical placement was printed without any overhanging issues and the detailed design and the fabrication flow of this assembled lens were described in Supplementary Fig. 11.

Discussion

To sum up, we've showcased an efficient micro-stereolithography method for rapid 3D printing of imaging lenses. By combining defocusing photopolymerization with a spin coating post-curing process, we eliminated pixelated surface imperfections from the conventional printing technique, all while maintaining fast production speeds. The technique has proven its ability to produce optical components with excellent surface smoothness (<1 nm), impressive precision (<1 μm), and consistent reproducibility, making it a robust solution for creating custom optical parts from optimized designs. These lenses not only have minimal distortion but also display outstanding optical clarity across the visible light spectrum. Multi-scale optical lenses with diameters ranging from 3 mm to 70 mm were successfully printed to verify the effectiveness of the proposed fabrication technique. An array of lenses can be fabricated in a single print, which can reduce the printing time for each lens to 3 minutes (Supplementary Fig. 4b). In summary, our findings spotlight the vast promise of 3D printing within the domain of optics, paving the way for innovative devices that could revolutionize freeform optics and optical imaging systems.

Here, we mainly modeled and fabricated axially symmetric optical lenses. Although more complex and functional lenses were printed with the desired results, such as lens array, CPC element, and lens assembly, further discussion and research are needed regarding the 3D printing parameters and quality. For non-axially symmetric-shaped lenses, additional mathematical modeling and simulation results are necessary to aid our 3D printing process. In terms of printing materials, we utilized HDDA-based high-transparency resin and various commercial clear resins. However, a further study with more focus on these photocurable materials should be done by investigating the optical properties. Through optical simulations in Zemax, we aim to manufacture more optimized lenses and lens combinations, such as achromatic lenses. New resin materials suitable for 3D printing optical devices also remain an open research question. Also, it would be very interesting to spin coat a different resin with different optical properties, such as refractive index and Abbe number. We anticipate such a lens with two materials might lead to even more advanced functions, such as anti-reflection, achromatic, or even reduced optical loss [44].

Methods

Photocurable Resin:

For the sample printing, the photocurable resin consists of 97 wt% 1,6-hexanedioldiacrylate (HDDA) as the monomer, and 1 wt% phenylbis (2,4,6-trimethylbenzoyl) phosphine oxide as the photoinitiator. A 2 wt% Avobenzone was used as a UV absorber to control the curing depth. They are purchased from Sigma-Aldrich (St. Louis, MO). The refractive index of this resin was measured as n = 1.463. Another transparent photocurable resin (high clear) was also employed, purchased from ANYCUBIC Technology Co., Ltd. China. The refractive index of this resin was measured as n = 1.50, which was close to the substrate material of Spherical lenses (Thorlabs, Inc.), N-BK7 glass (n = 1.515). Additionally, some other commercial clear resins were used to print the optical lenses to demonstrate the generality of the proposed fabrication process. The responding optical characteristics of photocurable resins were measured and plotted in Supplementary Fig. 7.

VPP-based 3D Printing System:

The VPP 3D printing system was customized to fabricate optical lenses (Fig. 2a). This system utilizes an 8K LCD screen as the dynamic mask with a maximum printing size of 165 × 72 mm^2 purchased from Phrozen Technologies LLC. This LCD screen contains 7680 × 4320 pixels with each pixel size of 22 × 22 μm^2. The building substrate was mounted on a precision motorized translation stage. The designed digital model was sliced into a number of 2D image patterns with 20 um thickness along the Z-Axis to build the sample. A 4A wavelength of 405 nm UV LED light source was employed as the light source. During the printing process, the LCD screen selectively allows the UV light to pass through to achieve different pattern projections. The UV light intensity that our system could provide was 3.09 mW/cm^2, measured by UV light meter (Chitu System). The projection module was mounted with a manual linear translation stage to achieve the vertical movement for defocusing image projection (Thorlabs). The printing settings were tested and optimized for our lens printing, which was demonstrated in Supplementary Table 2. The digital model was designed in SolidWorks and saved as STL files with maximum fine structures, minimizing the size of sliced triangles for better surface quality and structural precision in our lens fabrication (Supplementary Fig. 12). The slicing and printing codes of our system are performed in the MATLAB and UVtools.

Precision Spin Coating Method:

After the printing process, the sample printed on the glass slide was moved to a spin coater. The printed sample was centered and secured to the chuck using a vacuum. The liquid resin was manually dispensed onto the center of the printed sample, enough to cover the whole top surface. Then, the sample was spun at low speeds of 1000 rpm/min to spread the liquid resin for 20 seconds. The new uncured resin uniformly covered the printed sample and formed the demanded spherical surface, as shown in Fig 2b.

Post-Processing Method:

After spin coating, the fresh resin was uniformly distributed. To avoid the oxygen inhibition effect (Supplementary Fig. 13) on the liquid resin curing process, a customized post-curing device was used as shown in Fig. 2b. In this setup, a 405 nm 3W UV lamp was embedded in a vacuum chamber. The spin-coated sample on a glass substrate was put into the chamber. When the air pressure reached 29 inHg, the UV lamp was turned on for 40 seconds for post-curing. By utilizing different resins, the post-curing time was different. Then, the lens was peeled off from the glass printing substrate for the imaging and testing process. Some samples were also bonded with a quartz substrate (Oxford Instruments), which is highly transparent to UV light and widely used in optical components.

Bubble Avoid:

In VPP 3D printing, the bubble is a big issue during the curing process, which worsens the printing quality, surface performance, and mechanical properties, especially for bottom-up setup as shown in Supplementary Fig. 14. The bubbles come from (1) small bubbles in liquid resin self and (2) air trapped in between building platform and resin during layer separation. To avoid bubble issues, the fresh resin was first vacuumed for 30 minutes to make sure all small bubbles came out from the liquid and then slowly poured into the printing tank. For the printing process, after leveling calibration, the building platform moved down at the speed of 10 mm/min to the Zero position. Next, the building platform was moved up to 40 mm to manually check and remove the potential bubbles using a syringe. Then it directly moved back to the first layer height (20 um) and started the printing process. For lifting and retraction, the speed was set at 30 mm/min to avoid bubble generation when the sample was peeled off from the FEP film, creating bubbles randomly. For some large-scale lenses, we printed the samples in the off-center area of the building platform.

Optical Characterization of the 3D Printed Lenses:

The USAF 1951 resolution test target (R1DS1N, Thorlabs, Inc.) was used to evaluate the optical quality of the 3D-printed aspherical lens. For color-specific illumination, we used multiple bandpass filters with central wavelengths of 532 nm (FLH532-10, Thorlabs), 450 nm (FBH450-10, Thorlabs), and 650 nm (FBH650-10, Thorlabs) in the microscope. As depicted in Fig. 3a, we positioned the resolution test target at the lens's front focal plane. The images were then captured and analyzed using the inverted microscope setup. The camera recorded the images transmitted from the resolution target, allowing for subsequent analysis.

Surface Characterization of the 3D Printed Lenses:

Scanning Electron Microscopy (Teneo, FEI Company) images were acquired to capture the surface details. We used the voltage of 5 kV and the beam current of 10nA for the analysis. Initially, all samples were mounted to aluminum stubs using double-sided adhesive tape, then deposited with a gold layer through a Baltec SCD 005 vacuum sputter for 60 seconds at a 0.1 mbar vacuum before the SEM observation.

The surface roughness of the lens sample was measured using an Atomic Force Microscope (Asylum Cypher ES, Oxford Instruments). In our AFM measurements, a third order flattening function was implemented to address the curvature presented on the lens surface. Utilizing the tapping mode, surface metrology assessments were conducted using silicon AFM probes coated with aluminum for reflectivity enhancement. These probes exhibited a resonance frequency of 300 kHz and a force constant of 40 N/m.

An imaging system and scanning system were used to capture the 2D profiles of the printed samples to get the surface profile (Supplementary Fig. 5b and 5c). The designed and actual cross-section profiles were matched to record the printing errors. In addition, the 3D surface profiles of the lens sample were measured using a 3D Surface Metrology Microscope (Leica DCM8, Leica Microsystems), which unites the confocal microscopy and interferometry into one versatile. The Confocal RGB mode and the 10× objective lens was selected to measure the 3D surface with the optical resolution of 0.46 μm.

To measure the thickness of coating, we customized an imaging system (Supplementary Fig. 5b). We placed the printed sample in front of the imaging system. Before dropping the liquid resin, we took an image of the as-printed sample and leveraged an image processing approach to extract the as-printed profile, as shown in Figure 6a. Then we dropped the liquid and used a camera to capture a video of how the coating was gradually thinning out. After we obtained the video, we extracted the profile of the liquid frame by frame. Figure 6a shows the coating liquid at a specific frame. By dividing the diameter of the lens by the number of pixels it occurred, we computed the physical size of each pixel in the captured image. Then, we calculated the actual thickness of the coating in any location and compared it with the analytical and simulated results.

Simulation of Spin Coating

COMSOL Multiphysics was used to model and simulate the spin coating process. The simulation domain was set as 2D axisymmetric. The spin coating on substrates with layer stairs was modeled as a two-phase laminar flow with phase method. The spin coating on a smooth aspherical surface was modeled using a two-phase laminar flow with a moving mesh method. The viscosity and density of the coating resin were mentioned in the previous section. Liquid-gas interface was used for the two-phase interaction.

Supporting Information

Supporting Information is available from the Wiley Online Library or from the author.

Acknowledgements

This work was supported by the National Science Foundation (NSF) under grant number CMMI 2328362, CMMI 2318677, and the IUPUI initiative seed grant. Y.S. and J.H. contributed equally to this work. H.M. conceived the idea and directed this project. Y.S. designed and built the customized 3D printer, printed all the lenses, and conducted all the experiments. Y.S. and J. H. developed software code to control the printer. Y.S., J. H., and H.M. developed a theoretical model of precision spin coating. J.H. tested the surface roughness of all samples and set up optical systems. Y.S. and J.H. designed the structures and measured the profile data of lenses. Y.S. drafted the manuscript. H.M. reviewed and revised the manuscript.

Conflict of Interest

The authors filed a provisional patent for the proposed 3D printing method with spin coating.

References

[1] D. Gonzalez-Hernandez, S. Varapnickas, A. Bertoncini, C. Liberale, M. Malinauskas, *Advanced Optical Materials* **2023**, *11*, 2201701.

[2] S. Juodkazis, *Nature Photon* **2016**, *10*, 499.

[3] In *Optomechanical Systems Engineering*, John Wiley & Sons, Ltd, **2015**, pp. 35–56.

[4] T. Gissibl, S. Thiele, A. Herkommer, H. Giessen, *Nature Photon* **2016**, *10*, 554.

[5] S. Thiele, K. Arzenbacher, T. Gissibl, H. Giessen, A. M. Herkommer, *Science Advances* **2017**, *3*, e1602655.

[6] I. Gibson, D. Rosen, B. Stucker, M. Khorasani, *Additive Manufacturing Technologies*, Springer, Germany **2021**.

[7] A. Camposeo, L. Persano, M. Farsari, D. Pisignano, *Advanced Optical Materials* **2019**, *7*, 1800419.

[8] J. Baek, Y. Shan, M. Mylvaganan, Y. Zhang, X. Yang, F. Qin, K. Zhao, H. W. Song, H. Mao, S. Lee, *Advanced Materials* **2023**, *35*, 2304070.

[9] Y. Shan, P. Sahu, R. Sundararajan, H. Mao, *Proceedings of the ASME 2022 International Mechanical Engineering Congress and Exposition. Volume 2A: Advanced Manufacturing.* Columbus, Ohio **2022**.

[10] J. Hua, Y. Shan, H. Mao, *Proceedings of the ASME 2022 International Mechanical Engineering Congress and Exposition. Volume 2A: Advanced Manufacturing.* Columbus, Ohio **2022**.

[11] H. Mao, W. Jia, Y.-S. Leung, J. Jin, Y. Chen, *Rapid Prototyping Journal* **2021**, *27*, 861.

[12] L. Wu, Z. Dong, F. Li, H. Zhou, Y. Song, *Advanced Optical Materials* **2016**, *4*, 1915.

[13] F. Zhang, L. Zhu, Z. Li, S. Wang, J. Shi, W. Tang, N. Li, J. Yang, *Additive Manufacturing* **2021**, *48*, 102423.

[14] Y. Zhu, T. Tang, S. Zhao, D. Joralmon, Z. Poit, B. Ahire, S. Keshav, A. R. Raje, J. Blair, Z. Zhang, X. Li, *Additive Manufacturing* **2022**, *52*, 102682.

[15] A. Bagheri, J. Jin, *ACS Appl. Polym. Mater.* **2019**, *1*, 593.

[16] J. R. Tumbleston, D. Shirvanyants, N. Ermoshkin, R. Janusziewicz, A. R. Johnson, D. Kelly, K. Chen, R. Pinschmidt, J. P. Rolland, A. Ermoshkin, E. T. Samulski, J. M. DeSimone, *Science* **2015**, *347*, 1349.

[17] M. Regehly, Y. Garmshausen, M. Reuter, N. F. König, E. Israel, D. P. Kelly, C.-Y. Chou, K. Koch, B. Asfari, S. Hecht, *Nature* **2020**, *588*, 620.

[18] H. Quan, T. Zhang, H. Xu, S. Luo, J. Nie, X. Zhu, *Bioactive Materials* **2020**, *5*, 110.

[19] G. Shao, R. Hai, C. Sun, *Advanced Optical Materials* **2020**, *8*, 1901646.

[20] H. Xu, S. Chen, R. Hu, M. Hu, Y. Xu, Y. Yoon, Y. Chen, *Small* **2023**, *19*, 2300517.

[21] F. Alam, M. Elsherif, B. AlQattan, A. Salih, S. M. Lee, A. K. Yetisen, S. Park, H. Butt, *ACS Biomater. Sci. Eng.* **2021**, *7*, 794.

[22] F. Alam, A. E. Salih, M. Elsherif, A. K. Yetisen, H. Butt, *Additive Manufacturing* **2022**, *49*, 102464.

[23] Z. Hong, P. Ye, D. A. Loy, D. A. Loy, D. A. Loy, R. Liang, *Optica, OPTICA* **2021**, *8*, 904.

[24] J. Hua, Y. Shan, S. Wu, H. Mao, *Journal of Manufacturing Science and Engineering* **2023**, *146*, DOI 10.1115/1.4063137.

[25] F. Kotz, K. Arnold, W. Bauer, D. Schild, N. Keller, K. Sachsenheimer, T. M. Nargang, C. Richter, D. Helmer, B. E. Rapp, *Nature* **2017**, *544*, 337.

[26] E. Beckert, in *Inkjet Printing in Industry*, Wiley, Hoboken, NJ **2022**.

[27] Y. Shan, A. Krishnakumar, Z. Qin, H. Mao, *Additive Manufacturing* **2022**, *52*, 102653.

[28] Y. Shan, Y. Shui, J. Hua, H. Mao, *Journal of Manufacturing Processes* **2023**, *86*, 326.

[29] A. Zolfaghari, T. Chen, A. Y. Yi, *Int. J. Extrem. Manuf.* **2019**, *1*, 012005.

[30] C. Zhou, Y. Chen, *Journal of Manufacturing Processes* **2012**, *14*, 107.

[31] X. Chen, W. Liu, B. Dong, J. Lee, H. O. T. Ware, H. F. Zhang, C. Sun, *Advanced Materials* **2018**, *30*, 1705683.

[32] H. Gong, B. P. Bickham, A. T. Woolley, G. P. Nordin, *Lab Chip* **2017**, *17*, 2899.

[33] Y. Zhang, L. Wu, M. Zou, L. Zhang, Y. Song, *Advanced Materials* **2022**, *34*, 2107249.

[34] Y. Xu, P. Huang, S. To, L.-M. Zhu, Z. Zhu, *Advanced Optical Materials* **2022**, *10*, 2200488.

[35] Y. Pan, Y. Chen, *Additive Manufacturing* **2016**, *12*, 321.

[36] D. Aguirre-Aguirre, D. Gonzalez-Utrera, B. Villalobos-Mendoza, R. Díaz-Uribe, *Appl. Opt., AO* **2023**, *62*, C14.

[37] G. D. Berglund, T. S. Tkaczyk, *Opt. Express, OE* **2019**, *27*, 30405.

[38] R. Janusziewicz, J. R. Tumbleston, A. L. Quintanilla, S. J. Mecham, J. M. DeSimone, *Proc Natl Acad Sci USA* **2016**, *113*, 11703.

[39] C. Yuan, K. Kowsari, S. Panjwani, Z. Chen, D. Wang, B. Zhang, C. J.-X. Ng, P. V. y Alvarado, Q. Ge, *ACS Appl. Mater. Interfaces* **2019**, *11*, 40662.

[40] J. T. Toombs, M. Luitz, C. C. Cook, S. Jenne, C. C. Li, B. E. Rapp, F. Kotz-Helmer, H. K. Taylor, *Science* **2022**, *376*, 308.

[41] S. Peng, J. Xu, D. Li, J. Ren, M. Zhang, X. Wang, Y. Liu, *Int. J. Extrem. Manuf.* **2023**, *5*, 035007.

[42] B. G. Assefa, M. Pekkarinen, H. Partanen, J. Biskop, J. Turunen, J. Saarinen, *Opt. Express, OE* **2019**, *27*, 12630.

[43] S. Ristok, S. Thiele, A. Toulouse, A. M. Herkommer, H. Giessen, *Opt. Mater. Express, OME* **2020**, *10*, 2370.

[44] D. Astrauskytė, K. Galvanauskas, D. Gailevičius, M. Drazdys, M. Malinauskas, L. Grineviciute, *Nanomaterials* **2023**, *13*, 2281.